PCCP

PAPER

View Article Online
View Journal | View Issue

Cite this: *Phys. Chem. Chem. Phys.*, 2015, **17**, 25809

Diastereo-specific conformational properties of neutral, protonated and radical cation forms of (1*R*,2*S*)-*cis*- and (1*R*,2*R*)-*trans*-amino-indanol by gas phase spectroscopy†

Aude Bouchet,[a] Johanna Klyne,[a] Giovanni Piani,[bc] Otto Dopfer*[a] and Anne Zehnacker*[bc]

Received 29th January 2015,
Accepted 7th April 2015

DOI: 10.1039/c5cp00576k

www.rsc.org/pccp

Chirality effects on the intramolecular interactions strongly depend on the charge and protonation states. Here, the influence of chirality on the structure of the neutral, protonated, and radical cation forms of (1*R*,2*S*)-*cis*- and (1*R*,2*R*)-*trans*-1-amino-2-indanol diastereomers, prototypical molecules with two chiral centers, is investigated in a molecular beam by laser spectroscopy coupled with quantum chemical calculations. The neutral systems are structurally characterised by double resonance IR-UV spectroscopy, while IR-induced dissociation spectroscopy is employed for the charged molecules. The sterical constraints due to the cyclic nature of the molecule emphasise the chirality effects, which manifest themselves by the formation of an intramolecular hydrogen bond in neutral or protonated (1*R*,2*S*)-*cis*-amino-indanol. In contrast, this interaction is not possible in (1*R*,2*R*)-*trans*-amino-indanol. In the protonated species, chirality also influences the spectroscopic probes in the NH/OH stretch range by fine-tuning subtle effects such as the hyperconjugation between the σ(OH) orbital and σ* orbitals localised on the alicyclic ring. The radical cation undergoes opening of the alicyclic ring, which results in an ionisation-induced loss of the chirality effects.

1. Introduction

Stereochemistry plays an important role in the activity of biomolecules and their interaction with the environment. This is especially true for molecules bearing two adjacent chiral centres, which can be of identical or opposite chirality. The two diastereomers often possess distinct properties, in particular from a medicinal point of view. Methylphenidate, used for the treatment of hyperactivity, is especially illustrative in this respect as its activity is due to the form with the chiral centres of identical chirality, the other form being inactive.[1] In a similar fashion, antimalarial cinchona alkaloids like quinine are amino-alcohols with both amino and hydroxy groups borne by asymmetric carbons. In their active form, the substituents have opposite chirality.[2]

Gas-phase studies provide information on the structural differences between the diastereomers, without the complications imposed by the solvent.[3–10] The stereochemical effects observed in diastereomers isolated in the gas phase are often weak. Indeed most of the neutral systems studied so far like peptides,[11,12] polyols,[13] or amino-alcohols like neurotransmitters[14] and cinchona alkaloids[15,16] only display minor structural and spectroscopic differences. However, larger differences are observed between diastereomers interacting with a cation.[17] Cyclic systems stand out because the presence of the ring induces additional constraints, which may enhance the chirality effects.[18–20] For example, the two diastereomers of 1,2,3,4-tetrahydro-3-isoquinoline-methanol involve an OH···N or an NH···O interaction depending on the relative chirality of the adjacent asymmetric carbon and nitrogen atoms.[20,21]

Life chemistry involves species in different pH and redox states, which motivates the study of protonated or cationic species in parallel to that of the neutral. However, few comparative studies have been reported on stereochemical effects in different charge states to assess the sensitivity of stereochemical factors (enhancement or reduction) upon ionisation or protonation.[5,6,16,20]

This investigation compares the vibrational spectroscopy and structures of (1*S*,2*R*)-*cis*- and (1*R*,2*R*)-*trans*-1-amino-2-indanol

[a] *Institut für Optik und Atomare Physik, Technische Universität Berlin, Hardenbergstr. 36, D-10623 Berlin, Germany. E-mail: dopfer@physik.tu-berlin.de; Fax: +49 30 314 23018; Tel: +49 30 314 23017*
[b] *CNRS, Institut des Sciences Moléculaires d'Orsay (ISMO/UMR8214) and Univ. Paris Sud, Orsay, F-91405, France. E-mail: anne.zehnacker-rentien@u-psud.fr; Fax: +33 169 15 67 77; Tel: +33 169 15 39 33*
[c] *CLUPS (Centre Laser de l'Université Paris Sud/LUMAT FR 2764), Université Paris-Sud, Orsay, F-91405, France*

† Electronic supplementary information (ESI) available. See DOI: 10.1039/c5cp00576k

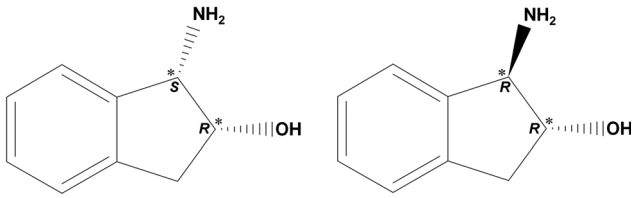

Scheme 1 Chemical structures of (1*S*,2*R*)-*cis*-AI (left) and (1*R*,2*R*)-*trans*-AI (right). Asterisks indicate the chiral centres.

isolated in a supersonic expansion, either neutral (AI), ionised (AI^+), or protonated (H^+AI). In this paper, *cis*- and *trans*-1-amino-2-indanol will be denoted by *cis*-AI and *trans*-AI, respectively (Scheme 1). The reason behind this choice of molecules is the presence of an amino-alcohol function, which is common to many important pharmaceutical compounds like neurotransmitters or antimalarial drugs.[14,22] *cis*-AI is indeed part of peptoids used as potent inhibitors of the HIV protease.[23] The efficiency of the antiviral drug demands proper stereochemistry of this sub-unit.[23] Moreover, the presence of an aliphatic ring is expected to enhance the differences between the two diastereomers. Neutral *cis*-AI has already been studied under jet-cooled conditions by means of Resonance-Enhanced Multiphoton Ionisation (REMPI) and double resonance vibrational spectroscopy.[24] Its hydrates[25] as well as its chiral recognition properties have also been investigated with the same experimental approach in the neutral ground state.[5,26] However, no spectroscopic and theoretical data are available for *trans*-AI and any of the radical cation or protonated species.

The aim of this work is to determine the structural differences due to chirality in the neutral molecules and to assess how they are modified upon ionisation or protonation, by investigating neutral, protonated, and radical cation species of the same chiral molecules with the same computational and spectroscopic techniques. To this end, we compare the structural information gained from IR-UV double resonance experiments on neutral *cis*- and *trans*-AI to those obtained by IR photodissociation for the radical cation and protonated forms using single-photon dissociation (IRPD) of Ar-tagged ions and/or IR multiple-photon dissociation (IRMPD) of the bare ions. Quantum chemical calculations are conducted as a support to the interpretation of the vibrational spectra.

2. Computational and experimental methods

2.1. Computational methods

The potential energy surfaces of neutral and protonated *cis*- and *trans*-AI are investigated by exploring the possible orientations of the OH and $NH_{2/3}$ groups around the C–O and C–N axes. The pseudo-equatorial (eq) and pseudo-axial (ax) orientations of these functional groups are also considered by varying their position relative to the median plane of the indane core of the molecule. Systematic initial calculations at the B3LYP/6-31G(d,p) level are performed for rotation of the OH and $NH_{2/3}$ groups, for the two possible positions of the functional groups, namely eq or ax. For the starting geometries of neutral *cis*-/*trans*-AI, steps of 90° and 120° are used for the OH and NH_2 groups, respectively. For protonated *cis*-/*trans*-H^+AI, the OH group has been rotated in steps of 60°. Hence, 24 geometries for each diastereomer of AI and 12 for each diastereomer of H^+AI are calculated at the B3LYP/6-31G(d,p) level.[27,28] The most stable ones are further optimised and their vibrational frequencies calculated at the dispersion-corrected B3LYP-D3/aug-cc-pVTZ level (Table 1).[29,30] All density functional calculations are performed using GAUSSIAN09.[31] The open-shell

Table 1 Calculated electronic (E_e), zero-point energy corrected (E_0) and free (ΔG) relative energies in kJ mol^{-1}, H-bond lengths (l_{NH-O} or l_{OH-N}) in Å, scaled harmonic frequencies in cm^{-1} and IR intensities of ν_{OH} and ν_{NH} in km mol^{-1} for AI, H^+AI and AI^+ calculated at the B3LYP-D3/aug-cc-pVTZ level

	OH conf.	$NH_{2/3}$ conf.	E_e	E_0	ΔG	l_{NH-O}	l_{OH-N}	ν_{OH}	ν_{NH} (as)[a]	ν_{NH} (as)[a]	ν_{NH} (s)[a]
Neutral											
cis-AI_I	eq	ax	0	0	0	—	2.059	3461 (108)	3427 (9)	—	3345 (3)
cis-AI_{II}	ax	eq	0.74	0.10	−0.23	—	2.048	3469 (104)	3455 (13)	—	3376 (3)
trans-AI_I	eq	eq	0	0	0	—	2.767	3613 (38)	3415 (4)	—	3335 (1)
trans-AI_{II}	eq	eq	4.03	3.26	2.80	2.941	—	3648 (39)	3410 (3)	—	3328 (1)
Protonated											
cis-H^+AI_I	eq	ax	0	0	0	2.057	—	3670 (131)	3368 (81)	3319 (74)	3219 (71)
cis-H^+AI_{II}	ax	eq	4.54	4.60	4.36	1.889	—	3669 (115)	3361 (71)	3310 (75)	3164 (112)
trans-H^+AI_I	eq	eq	0	0	0	2.681	—	3655 (103)	3343 (74)	3320 (83)	3244 (41)
trans-H^+AI_{II}	eq	eq	4.94	4.61	4.06	2.722	—	3641 (69)	3342 (75)	3314 (81)	3239 (43)
Radical cation											
AI^+_I	—	—	0	0	0	—	—	3613 (247)	3521 (84)	—	3409 (175)
AI^+_{II}	—	—	2.66	0.74	0.74	—	—	3627 (350)	3523 (92)	—	3417 (317)
AI^+_{III}	—	—	2.43	3.00	3.44	—	—	3569 (75)	3518 (88)	—	3407 (178)
AI^+_{IV}	—	—	4.67	4.52	4.53	—	—	3621 (225)	3518 (88)	—	3405 (170)
AI^+_V	—	—	5.37	4.64	4.90	1.786	—	3654 (179)	3456 (218)	—	3157 (366)
AI^+_{VI}	—	—	10.27	9.50	9.14	—	—	3644 (144)	3448 (220)	—	2981 (449)
AI^+_{VII}	—	—	11.49	10.34	9.93	—	—	3641 (161)	3451 (226)	—	3091 (452)
AI^+_{VIII}	—	—	0.69	4.83	9.41	1.780	—	—	3351 (62)	3293 (74)	3022; 3017 (184; 188)

[a] as and s indicate the asymmetric and symmetric NH stretch vibrations.

radical cations are calculated at the unrestricted level (UB3LYP), and spin contamination is found to be negligible. Because of insufficient agreement between the experimental IRPD spectra of H^+AI–Ar and the spectra calculated for H^+AI, the properties of H^+AI–Ar complexes have also been calculated. Because of the high flexibility of the open form of the AI^+ radical cations (*vide infra*), their potential energy surface is initially explored by molecular dynamics (MD) simulations. For this purpose, the AMBER force field is employed in the NVE ensemble, at a temperature defining the initial velocities of 500 K, as implemented in the Gabedit software.[32] Subsequently, geometry optimisation and frequency calculations are performed at the B3LYP-D3/aug-cc-pVTZ level for the 32 most stable isomers resulting from this exploration. All reported energies are corrected for zero point energy. Moreover, all binding energies of the Ar-tagged complexes are corrected for basis set superposition error.

The vibrational spectra of the stable structures are convoluted by a Lorentzian line shape of 3 cm^{-1} full width at half-maximum (FWHM) in the 3 μm range and 10 cm^{-1} in the fingerprint range, which accounts for the respective experimental resolution achieved. The harmonic frequencies of neutral AI are scaled by 0.955 to fit the experimental data of *cis*-AI.[24] Scaling factors of 0.96 and 0.98 are applied to the frequencies of the ionic species in the 3 μm and fingerprint ranges, respectively, to improve the agreement with the experimental spectra. All calculated frequencies given in the text, figures and Table 1 include the scaling factor.

Visualisation of hydrogen bonds (H-bonds) is achieved by means of the non-covalent interaction (NCI) technique.[33] Details of this method and its application to intramolecular H-bonds have been described recently.[33–35] Briefly, the NCI technique rests on the topological analysis of the electron density ρ and its reduced gradient $s(\rho)$ in regions of weak electron density and small reduced gradient. The zones where $s(\rho)$ is close to zero, *i.e.* close to minima of electron density, are characteristic of non-covalent interactions. The visualisation is accomplished by plotting iso-surfaces of the reduced gradient and rests on a RGB colouring scheme to rank the interactions using the sign of the second eigenvalue, λ_2, of the Hessian matrix. Red iso-surfaces correspond to positive λ_2, *i.e.* repulsive regions, while blue iso-surfaces correspond to negative λ_2, *i.e.* regions corresponding to favourable interactions. Green iso-surfaces correspond to weak delocalised interactions, *i.e.* regions where λ_2 is almost zero.

2.2. Experimental methods for the neutral AI molecules

Electronic and vibrational spectra of neutral AI are recorded in a supersonic jet by expanding *cis*- or *trans*-AI seeded in helium (~3 bar) through a 300 μm pulsed nozzle into a chamber maintained at 10^{-6} mbar. The experimental setup in Orsay has been described in detail elsewhere.[36–40] The *cis*- and *trans*-AI samples (>99%) are contained in an oven heated to ~410 or ~360 K, respectively. Mass-resolved S_0–S_1 spectra are obtained by means of one-color REMPI. The supersonic beam crosses the slightly focused UV laser (4 m focal length) in the ion-source region of a linear one-meter time-of-flight mass spectrometer. The ions are detected using a microchannel plate detector.

Vibrational spectra are obtained using the IR-UV double resonance technique.[41–43] To this end, two counter propagating synchronised laser beams are focused on the cold region of the supersonic expansion. The UV probe laser is fixed on each of the main transitions observed in the S_0–S_1 spectrum, while the IR pump laser is scanned in the range of interest. Absorption of the IR photons is measured as a dip in the ion current induced by the UV probe, allowing for the measurement of mass-resolved conformer-selective vibrational IR spectra.

The UV radiation is generated by mixing the frequency-doubled output of a dye laser with the fundamental radiation of its Nd:YAG pump laser. The wavelength calibration is achieved using a wavemeter. The tuneable IR source is an optical parametric oscillator (IR-OPO) laser based on a KTP crystal. The IR pulse is fired 50 ns before the UV pulse and focused by a lens with 0.5 m focal length. The resolution of the UV laser is 0.02 cm^{-1}, while that of the IR-OPO laser is 3 cm^{-1}.

2.3. Experimental methods for the ionic systems

2.3.1. Infrared photodissociation (IRPD). The vibrational spectra of the H^+AI and AI^+ ionic species are recorded in the 3 μm range (2800–3800 cm^{-1}) using the messenger technique[44,45] by single photon IRPD spectroscopy of mass-selected H^+AI–Ar or AI^+–Ar cluster ions in a tandem quadrupole mass spectrometer in Berlin, which is coupled to an electron impact ionisation source and an octopole ion trap.[46,47] A pulsed supersonic plasma expansion is generated by electron and chemical ionisation, and subsequent clustering reactions of the ions occur in the high-pressure regime of this expansion. The expanding gas mixture is produced by passing Ar carrier gas (2–6 bar) through a reservoir filled with *cis*- or *trans*-AI heated to 410 and 385 K, respectively. Cluster ions are mass selected by the first quadrupole and irradiated in an adjacent octopole with a tunable IR laser pulse. The excitation of vibrational resonances induces the evaporation of the Ar ligand, which is the only fragmentation channel observed. The fragment ions are selected by the second quadrupole and monitored using a Daly detector as a function of the laser frequency to obtain the IRPD spectra of the parent clusters. The IR laser beam is generated using an IR-OPO pumped by a nanosecond Q-switched Nd:YAG laser, with a pulse energy of 2–5 mJ in the 2800–3700 cm^{-1} range, a repetition rate of 10 Hz, and a bandwidth of 1 cm^{-1}. The calibration of the IR laser frequency is accomplished using a wavemeter. To establish and confirm the composition of a given cluster ion, collision-induced dissociation (CID) spectra are recorded. For this purpose, the octopole is filled with N_2 up to 10^{-5} mbar, resulting in collisions with ~10 eV collision energy in the laboratory frame. Recent applications of this IRPD approach of tagged ions in the Berlin laboratory include hydrocarbon ions,[48–57] silicon-containing ions,[58–60] and biological molecules and their hydrates.[61–66]

2.3.2. Infrared multiple photon dissociation (IRMPD). The IR spectra of isolated *cis*- and *trans*-H^+AI are obtained in the fingerprint range (900–1800 cm^{-1}) by means of IRMPD spectroscopy. The spectra are recorded in a Fourier transform ion

cyclotron resonance (FT-ICR) mass spectrometer equipped with an electrospray ion source and coupled to the IR beamline of a tunable free electron laser (FEL) at the CLIO (Centre Laser Infrarouge d'Orsay) facility in Orsay.[67] H^+AI ions are produced by spraying a 10^{-3} M solution of *cis*- or *trans*-AI dissolved in MeOH/H_2O (4 : 1) at a flow rate of 120 μL min^{-1}. The produced ions are accumulated in a hexapole ion trap for 1 s and transferred into the ICR trap *via* an octopole ion guide. Subsequently, the H^+AI ions are mass selected and irradiated for 1 s. Typical average powers of the FEL operating at 25 Hz are about 1.5 W at 1000 cm^{-1} and 0.7 W at 1800 cm^{-1}. The bandwidth of the FEL radiation (FWHM) is of the order of 0.5% of the central wavelength, which corresponds to 5 cm^{-1} at 1000 cm^{-1}. The calibration of the wavelength is achieved *via* the spectrum of a polystyrene film. The step size employed is ~4 cm^{-1}. The only fragmentation channel observed upon IRMPD of *cis*- and *trans*-H^+AI (*m*/*z* 150) is *m*/*z* 133, corresponding to loss of NH_3, which can be explained in terms of stereochemical constraints within the molecules.[68] Parent and fragment ion intensities are monitored as a function of the laser frequency, and the IRMPD efficiency is then calculated as $R = -\log(I_{parent}/I_{total})$, in which I_{parent} is the parent ion intensity and I_{total} the sum of the parent and fragment ion intensities. Recent applications of the IRMPD approach at CLIO from our groups include hydrocarbon ions,[69] protonated neurotransmitters,[70] metal–organic complexes,[71–73] and chiral recognition studies.[5,74,75]

3. Results

3.1. Computational results

3.1.1. Neutral AI molecules. Fig. 1 displays the most stable calculated structures of *cis*- and *trans*-AI. *cis*-AI occurs in two almost isoenergetic conformers, denoted *cis*-AI_I and *cis*-AI_{II}, which have been studied before.[24,25] The previous B3LYP/6-31G** calculations indicate that the most stable form, *cis*-AI_I, displays OH and NH_2 substituents in eq and ax positions (eq–ax), respectively. The slightly less stable conformer has the opposite conformation resulting from the ring inversion, with OH and NH_2 substituents in ax and eq positions (ax–eq), respectively. Only these two conformers are found below 10 kJ mol^{-1}.[24,25] Our calculations performed at the B3LYP-D3/aug-cc-pVTZ level (*i.e.*, with a larger basis set and including dispersion) lead to similar conclusions. At this level, *cis*-AI_{II} is hardly higher in energy (0.1 kJ mol^{-1}) than *cis*-AI_I. Both conformers have an intramolecular H-bond of comparable strength, as shown by similar OH···N distances of 2.059/2.048 Å for *cis*-$AI_{I/II}$. The NCI plots for *cis*-AI_I and *cis*-AI_{II} in Fig. 1 both show the bicoloured iso-surface typical of the intramolecular H-bond. The red part of this iso-surface, like the red disk-shaped iso-surfaces located at the centre of each ring, is the signature of the ring closure while the blue part characterises the favourable H-bond interaction. The additional iso-surface observed in *cis*-AI_{II} (NH···CH) is not significant as the reduced gradient is very close to zero: its sign becomes unstable, which makes it impossible to assign the zone to either attraction or repulsion.[35]

In contrast to *cis*-AI, *trans*-AI can adopt many more conformations below 10 kJ mol^{-1} (Fig. 1 and Fig. S1 in the ESI†). We find eight conformers, which is a sign of a less constrained molecule. In the four most stable forms, both substituents are in the equatorial position (eq–eq). The first conformer with both substituents in the axial position, namely *trans*-AI_V, is higher in energy by 8.6 kJ mol^{-1} compared to *trans*-AI_I. None of these conformers has a H-bond, as evidenced by the long OH···N distances (*e.g.*, 2.767 Å for the most stable *trans*-AI_I conformer) and the NCI plot in Fig. 1, which explains the less constrained geometry along the COH and CNH_2 torsions. In contrast, ring inversion causes a much higher energy difference in *trans*-AI than in *cis*-AI, as expected from the known equatorial preference of the substituents.

3.1.2. Protonated AI molecules (H^+AI). The amino group of AI is by far the most stable site of protonation, as is well known for aromatic amino-alcohols.[76] Indeed, the methylamine fragment has a higher proton affinity (899 kJ mol^{-1}) than the ethanol (776.4 kJ mol^{-1}) and benzene (750.4 kJ mol^{-1}) fragments.[77]

Similar to neutral AI, the main structural difference between *cis*- and *trans*-H^+AI is the ability of *cis*-H^+AI to form an intramolecular H-bond between the NH_3^+ and OH groups. *cis*-H^+AI has the same two conformers as the neutral form (Fig. 2), with the same energetic order. However, the difference in energy between *cis*-H^+AI_I and *cis*-H^+AI_{II} (4.6 kJ mol^{-1}) is much larger than in the neutral molecule (0.1 kJ mol^{-1}). In the most stable *cis*-H^+AI_I isomer, the $NH_{ax}\cdots O_{eq}$ distance amounts to 2.057 Å, while it is much shorter in the less stable *cis*-H^+AI_{II} isomer ($NH_{eq}\cdots O_{ax}$ = 1.888 Å). Therefore it seems that the more stable form displays the weaker H-bond, corresponding to the longer NH···O distance, a point to which we shall return in Section 4.

In contrast to *cis*-H^+AI, five low-energy minima are found for *trans*-H^+AI (Fig. 2 and Fig. S2 in the ESI†). Similar to the neutral

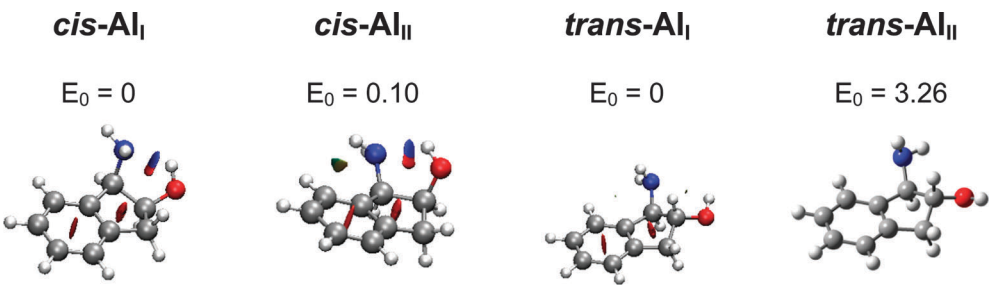

Fig. 1 Most stable structures and NCI plots of *cis*- and *trans*-AI calculated at the B3LYP-D3/aug-cc-pVTZ level. Relative energies are given in kJ mol^{-1}.

molecule, the two most stable ones, *trans*-H^+AI_I and *trans*-H^+AI_{II}, have both OH and NH_3^+ groups in the equatorial position. They only differ by the rotation of the OH group. The three higher energy conformers, *trans* H^+AI_{III-V}, are more than 10 kJ mol^{-1} less stable than *trans*-H^+AI_I and have their functional groups in the axial position. As for the neutral molecule, the *trans* conformation prevents the formation of an intramolecular H-bond in H^+AI.

The NCI analysis of the most stable conformers in Fig. 2 visualises the differences between *cis*- and *trans*-H^+AI on the one hand and *cis*-H^+AI_I and *cis*-H^+AI_{II} on the other hand. The bicoloured iso-surface typical of the intramolecular H-bond is clearly observed for *cis*-H^+AI while it is absent for *trans*-H^+AI. The red and blue colours of the iso-surface are more pronounced in *cis*-H^+AI_{II} than in *cis*-H^+AI_I, as expected for its stronger H-bond, which in turn induces more steric constraints. The electronic density at the critical point confirms this visual observation. While in the repulsive part the ring strain due to the benzene and alicyclic rings appears at the same positive values of $\sim$0.020 and 0.035 a.u., the two *cis*-H^+AI conformers differ by the electronic density at the critical points characteristic of the H-bonds. In both positive and negative λ_2 regions, the electronic density is higher for *cis*-H^+AI_{II} (0.031 *vs.* 0.023 a.u. and 0.039 *vs.* 0.020 a.u.).

3.1.3. Radical AI^+ cations. Systematic exploration of the potential energy surface of the open-shell *cis*- and *trans*-AI^+ radical cations evidences the planarity of the NH_2 group ($sp^3 \rightarrow sp^2$ hybridisation) accompanied by opening of the aliphatic ring due to the cleavage of the NC–CO bond. This cleavage occurs for both the equatorial and axial conformations of the substituents, and for both the *cis* and *trans* forms of the radical cation. Such a ring opening upon ionisation has already been described for indane derivatives, like 2-indanol, giving rise to distonic ions.[78] In AI^+, the formation of the non-cyclic distonic ion causes the loss of chirality. The formed distonic ions are therefore identical, independent of whether initially produced from the *cis* or *trans* form.

Once the aliphatic ring is open, the system is much more flexible since the two resulting side chains (HC–NH_2 and H_2C–CHOH) can adopt many different conformations. The potential becomes much richer with several minima close in energy and separated by low barriers. The exploration using AMBER results in 32 stable structures, which have subsequently been optimised at the B3LYP-D3/aug-cc-pVTZ level. The eight most stable conformers are presented in Fig. 3 and can be classified into three families. For structures denoted AI^+_I to AI^+_{VII}, the NBO analysis reveals that the excess positive charge is mainly localised on the HC–NH_2 chain (iminium, 0.51–0.71 e for I–VII), and the OH-bearing carbon atom carries most of the spin (Mulliken spin density 0.42–0.90). Among these isomers, the four low-lying AI^+ geometries (AI^+_{I-IV}, $E_0 \leq 4.6$ kJ mol^{-1}) make up the first class of AI^+ structures, which do not allow for

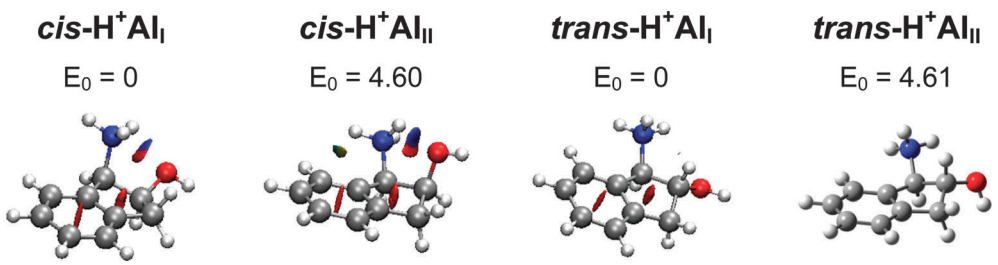

Fig. 2 Most stable structures and NCI plots of *cis*- and *trans*-H^+AI calculated at the B3LYP-D3/aug-cc-pVTZ level. Relative energies are given in kJ mol^{-1}.

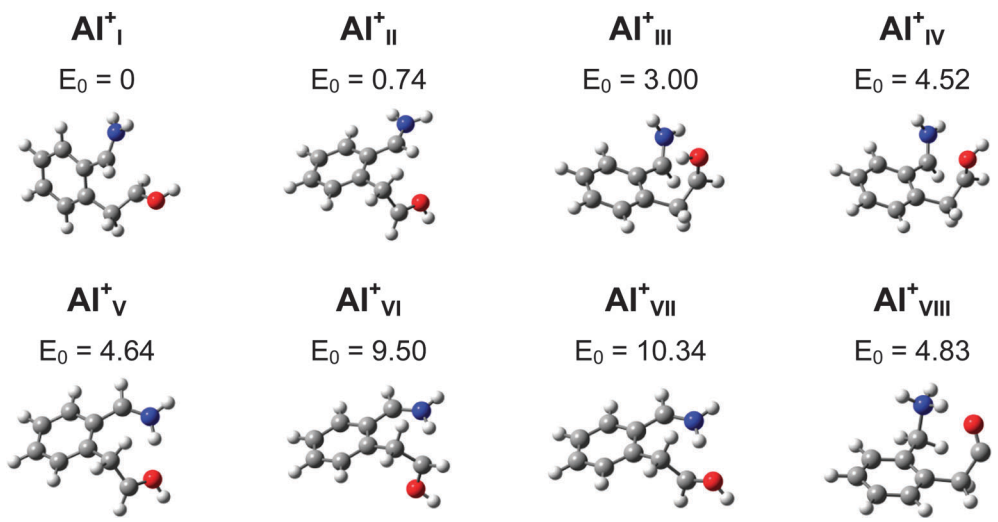

Fig. 3 The eight most stable geometries of the radical cation AI^+ found within $D_0 \sim 10$ kJ mol^{-1} calculated at the B3LYP-D3/aug-cc-pVTZ level.

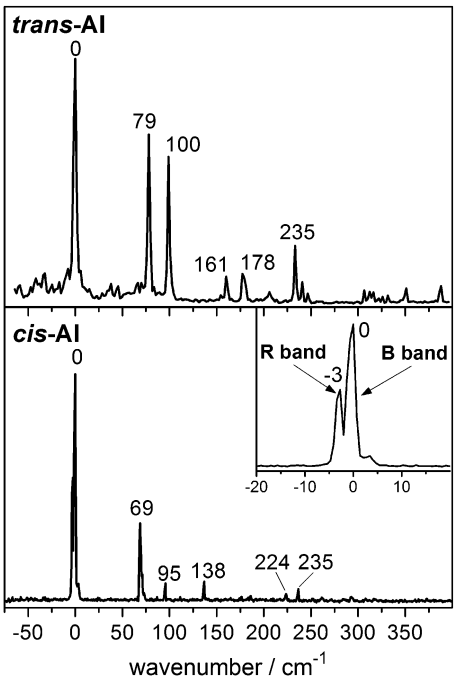

Fig. 4 S_0–S_1 electronic spectra of jet-cooled *cis*-AI[17] (bottom) and *trans*-AI (top) recorded at *m*/*z* 149. The inset shows the transition origin of *cis*-AI with the doublet structure R/B assigned to the two conformers I/II. The wavenumber scale is relative to the transition origin of each diastereomer at 36 915 cm^{-1} for *cis*-AI and 37 017 cm^{-1} for *trans*-AI.

the formation of an intramolecular H-bond. Secondly, structures denoted $AI^+_{V–VII}$ ($4.6 \leq E_0 \leq 10.4$ kJ mol^{-1}) have H-bonds between the iminium group and the radical site. Third, a proton transfer from the OH group to the NH_2 group is observed in the keto conformer AI^+_{VIII}, which is found at E_0 = 4.8 kJ mol^{-1}. For this third class of conformers, the positive charge is localised on the NH_3 group (ammonium, 0.89 e) and the spin on the carbon atom bearing the keto group (spin density 0.69).

3.2. Electronic and vibrational spectroscopy of neutral AI

The electronic spectroscopy of *cis*-AI has already been reported.[24] Briefly, the S_0–S_1 transition origin in Fig. 4 consists of a doublet at 36 918 (B) and 36 915 cm^{-1} (R). The splitting has been explained by the presence of two almost isoenergetic conformers, *cis*-AI_I and *cis*-AI_{II}, based on IR-UV fluorescence dip experiments.[24] On the basis of dispersed emission spectra, the vibronic bands observed at 69 and 95 cm^{-1} have been assigned to low-frequency modes of the most stable *cis*-AI_I, responsible for the B origin.

The S_0–S_1 electronic spectra of *cis*- and *trans*-AI are very close to each other (Fig. 4). The transition origin of *trans*-AI appears at 37 017 cm^{-1}, about 100 cm^{-1} higher in energy than those of the two *cis*-AI isomers. These values are very close to those reported for 2-indanol (37 019 cm^{-1}),[79] 1-amino-indane (36 947 and 37 064 cm^{-1} for the axial and equatorial conformers, respectively),[80] and indane (36 904 cm^{-1}).[81] This observation shows that neither the presence of the NH_2 or OH group nor the *cis* or *trans* character of the molecule strongly influences the electronic transition localised on the phenyl ring. The main difference in *trans*-AI relative to *cis*-AI is that there is no indication of the presence of a second conformer. Indeed, changing the carrier gas from helium to neon or argon does not modify the relative intensities observed in the spectrum. Vibronic bands appear at similar frequencies as for *cis*-AI. The vibronic bands of *trans*-AI observed at 79 and 100 cm^{-1} are assigned to the puckering and the butterfly motions (calculated values of 90 and 134 cm^{-1} in S_0 for *trans*-AI_I), and the bands at 161 and 178 cm^{-1} are overtone and combination bands of the former. The two fundamentals are slightly higher in frequency relative to *cis*-AI, where they appear at 69 and 95 cm^{-1} (calculated values of 83 and 124 cm^{-1} in S_0 for *cis*-AI_I). Moreover, the origin transition is significantly less pronounced relative to the

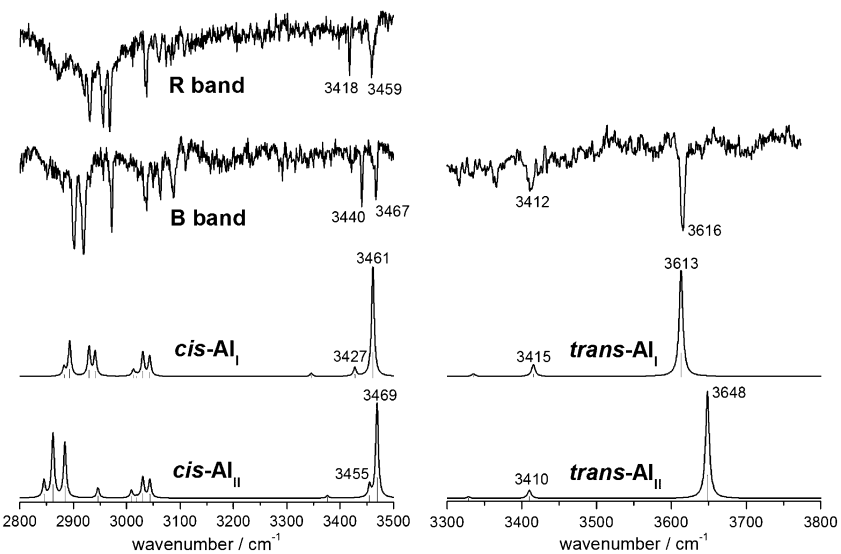

Fig. 5 IR-UV double resonance spectra of jet-cooled *cis*-AI[17] (left) and *trans*-AI (right) compared to the vibrational IR absorption spectra of the most stable conformers calculated at the B3LYP-D3/aug-cc-pVTZ level.

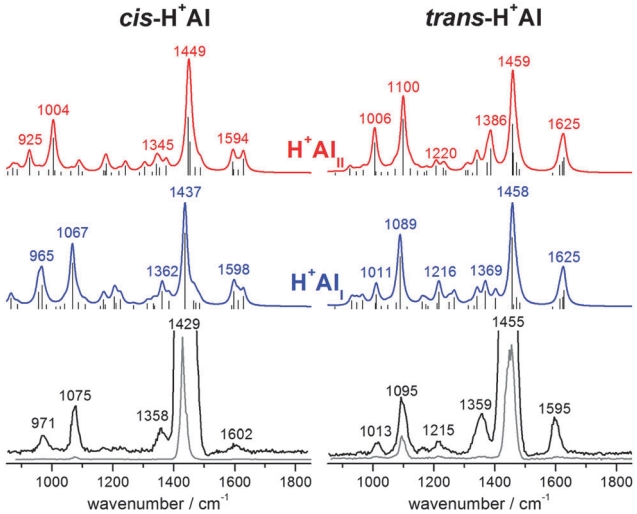

Fig. 6 IRMPD spectra of *cis*-H^+AI (left) and *trans*-H^+AI (right) monomers compared to the vibrational IR absorption spectra of the most stable conformers calculated at the B3LYP-D3/aug-cc-pVTZ level. Unsaturated spectra are obtained by decreasing the irradiation time in the ICR cell from 1 s (black lines) to 200 ms (grey lines).

other vibronic bands in *trans*-AI, indicating a larger modification of the potential energy surface upon electronic excitation.

The vibrational spectrum of *trans*-AI is compared in Fig. 5 to those previously obtained for the two conformers of *cis*-AI.[24] The IR-UV double resonance spectra recorded using the UV laser fixed on the six most intense peaks observed in the UV spectrum of *trans*-AI are all the same, which confirms the presence of a single isomer. They show a single OH stretch band (ν_{OH} = 3616 cm^{-1}) and a much weaker band assigned to the NH_2 asymmetric stretch ν_{NH} at 3412 cm^{-1}. This vibrational pattern can easily be assigned to the most stable *trans*-AI_I conformer by considering the calculated IR absorption spectra of the lowest lying eq–eq and ax–ax isomers. For this conformer, ν_{OH} is calculated at 3613 cm^{-1} and ν_{NH} at 3415 cm^{-1}. The spacing between the two peaks of *trans*-AI_{II} does not reproduce the experimental data with the same accuracy. In contrast, the vibrational spectra recorded by setting the UV probe frequency on the two components of the R/B doublet observed for *cis*-AI differ from each other.[24] Their ν_{OH} bands appear at 3459 and 3467 cm^{-1} and their ν_{NH} transitions at 3418 and 3440 cm^{-1} for the R and B origin, respectively. Hence, ν_{OH} is observed in very different spectral ranges for the *cis* and *trans* diastereomers. While its frequency is typical of a free OH group in *trans*-AI, both *cis*-AI conformers have an intramolecular OH···N interaction. The similar ν_{OH} frequencies show that the intramolecular H-bonding is almost the same in the two *cis*-AI conformers.[24,35] The ν_{NH} band appears at a similar frequency in *trans*-AI (3412 cm^{-1}) and *cis*-AI_I (3418 cm^{-1}). *cis*-AI_{II} stands out with a much higher value (3440 cm^{-1}), a point that will be discussed in Section 4.

3.3. Vibrational spectroscopy of protonated AI (H^+AI)

3.3.1. IRMPD spectra in the fingerprint range. The IRMPD spectra of *cis*- and *trans*-H^+AI in Fig. 6 show noticeable differences in their frequencies and intensity ratios for several vibrational bands. The spectra are dominated by a strong transition in the 1420–1460 cm^{-1} range. Unsaturated spectra obtained by decreasing the irradiation time in the ICR cell from 1 s to 200 ms yield the position of this transition as 1429 cm^{-1} for *cis*-H^+AI and 1455 cm^{-1} for *trans*-H^+AI. Moreover, the peak near 1100 cm^{-1} is red shifted by 20 cm^{-1} for *cis*-H^+AI (1075 cm^{-1}) relative to *trans*-H^+AI (1095 cm^{-1}), as well as the one observed near 1000 cm^{-1} (shifted by 42 cm^{-1}). The peak observed at 1358/9 cm^{-1} is almost the same for both diastereomers and the band located at around 1600 cm^{-1} is found significantly broader for *cis*-H^+AI.

3.3.2. IRPD spectra in the 3 μm range. The IRPD spectra of the *cis*-H^+AI–Ar and *trans*-H^+AI–Ar clusters shown in Fig. 7 reveal four major peaks easily assigned to the ν_{OH} and three ν_{NH} stretches. Surprisingly, the ν_{OH} vibration appears at higher frequency when the OH group is involved as a proton acceptor in the H-bond. It is observed at 3670 cm^{-1} for *cis*-H^+AI–Ar and

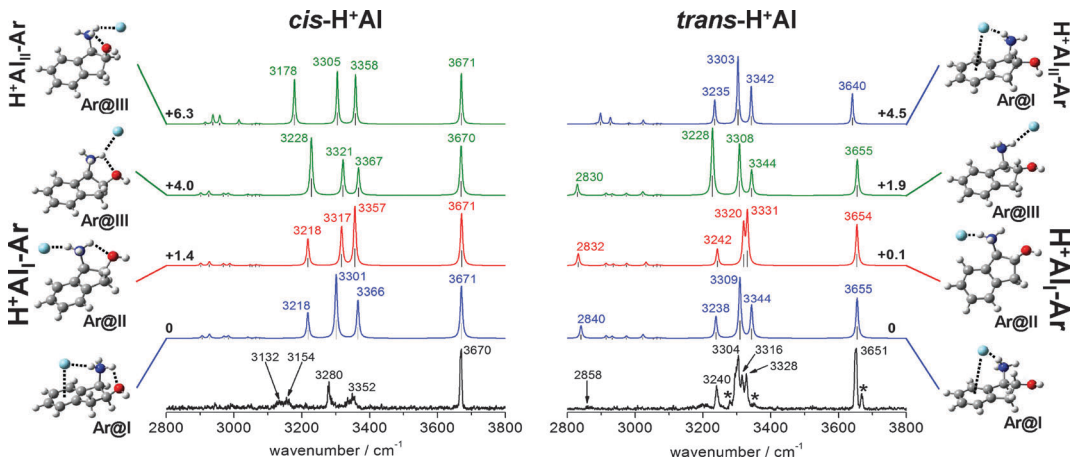

Fig. 7 IRPD spectra of *cis*-H^+AI–Ar (left) and *trans*-H^+AI–Ar (right) compared to the vibrational IR spectra of the most stable Ar complexes of each diastereomer (with Ar@NH_I in blue, Ar@NH_{II} in red and Ar@NH_{III} in green) calculated at the B3LYP-D3/aug-cc-pVTZ level. Peaks indicated by asterisks in the experimental spectrum of *trans*-H^+AI–Ar are due to a contamination of *cis*-H^+AI–Ar. Relative energies with respect to the most stable *cis*- or *trans*-H^+AI–Ar complex in kJ mol^{-1} are indicated on each spectrum.

at 3651 cm^{-1} for *trans*-H^+AI–Ar. The three ν_{NH} modes also reveal spectral differences between *cis*- and *trans*-H^+AI–Ar. The asymmetric ν_{NH} bands occur between 3304 and 3328 cm^{-1} for *trans*-H^+AI–Ar, while they are observed at 3280 and 3352 cm^{-1} for *cis*-H^+AI–Ar. The symmetric ν_{NH} band is found at 3240 cm^{-1} for *trans*-H^+AI–Ar and appears as a broad doublet at 3154 and 3132 cm^{-1} for *cis*-H^+AI–Ar. This latter feature is strongly red shifted compared to the one of *trans*-H^+AI–Ar, confirming the presence of the intramolecular H-bond with NH_3^+ as a proton donor.

Additional small peaks, marked with asterisks in Fig. 7, are also observed in the spectrum of *trans*-H^+AI–Ar at 3670, 3352, and 3280 cm^{-1}, which correspond to those characteristics of the *cis* diastereomer. These features are then assigned to a *cis* contaminant present in the *trans* sample.

3.3.3. Conformational assignment. The linear IR absorption spectrum predicted for the *cis*-H^+AI_I conformer shows satisfactory agreement with the IRMPD spectra measured in the fingerprint range (Fig. 6). In particular, the peaks located at 1358, 1075 and 971 cm^{-1} in the experimental spectrum, assigned to an aliphatic CH bending mode, the CO stretch, and a coupled mode mainly involving an aromatic out-of-plane CH bend and deformation of the substituents, are close to the calculated frequencies of 1362, 1067 and 965 cm^{-1}, respectively. The intense peak observed at 1429 cm^{-1} is assigned to the NH_3 umbrella inversion calculated at 1437 cm^{-1}. The weak and broad bands located at 1602 cm^{-1} are mainly attributed to the asymmetric NH_3 bend coupled to the phenyl C–C stretch mode 8b (Wilson notation),[82] predicted at 1598 cm^{-1}. Thus, all significant transitions show deviations of less than 10 cm^{-1} between the experimental IRMPD and simulated IR spectrum of *cis*-H^+AI_I, which is of the order of the spectral resolution of 10 cm^{-1}. In contrast, the IRMPD spectrum is not consistent with the IR spectrum predicted for the *cis*-H^+AI_{II} conformer, especially for the most intense peaks predicted at 1449, 1004, and 925 cm^{-1}, with deviations of 20, 71, and 46 cm^{-1}, respectively. The analysis of the IRMPD spectrum of *cis*-H^+AI indicates the predominance of the *cis*-H^+AI_I isomer at room temperature, with at most minor population of the less stable *cis*-H^+AI_{II} isomer.

In the 3 μm range, the comparison of the experimental IRPD spectrum of *cis*-H^+AI–Ar with those calculated for *cis*-$H^+AI_{I/II}$ (Fig. S3 in the ESI†) immediately reveals that the Ar ligand substantially affects the spectrum.[83–88] Hence, Ar complexation must be taken into account in the calculations. To this end, geometries and vibrational frequencies of the *cis*-$H^+AI_{I/II}$–Ar clusters (Fig. 7 and Fig. S5 in the ESI†) have been calculated. It turns out that the preferred Ar binding site for both conformers is indeed the NH_3^+ group with a NH···Ar contact.[83–88] For *cis*-H^+AI_I–Ar, the preferred Ar binding site is the NH group pointing toward the phenyl ring (Ar@NH_I), because Ar benefits from the additional attractive dispersion interaction with the aromatic π-electrons.[89] The second and third most stable isomers correspond to Ar binding to the NH group pointing away from the molecule (Ar@NH_{II}) and to that involved in the NH···O H-bond (Ar@NH_{III}). The corresponding Ar binding energies are 11.2, 9.8 and 7.2 kJ mol^{-1}, respectively. Clusters of *cis*-H^+AI_{II}–Ar are found at least 6.3 kJ mol^{-1} higher in energy than that of the most stable *cis*-H^+AI_I–Ar conformer, which corresponds to a significant increase of the energy gap between *cis*-H^+AI_I and *cis*-H^+AI_{II} induced by the Ar tagging.

In the three *cis*-H^+AI_I–Ar complexes described above, ν_{OH} is not affected by Ar complexation. On the other hand, the spacing observed between the two asymmetric ν_{NH} modes (72 cm^{-1}) is well reproduced only by the Ar@NH_I cluster (65 cm^{-1}), which is the most stable *cis*-H^+AI_I–Ar isomer. This spacing is predicted to be only 40 and 46 cm^{-1} for Ar@NH_{II} and Ar@NH_{III}, so that these isomers can be excluded. The broad peak observed near 3150 cm^{-1} assigned to the H-bonded ν_{NH} mode is about 70 cm^{-1} lower than the value predicted for Ar@NH_I. However, as none of the Ar binding sites for *cis*-$H^+AI_{I/II}$ induce such a large red shift of this mode, this effect is probably related to a larger anharmonicity of the H-bonded ν_{NH}. The preferred Ar binding site to *cis*-H^+AI_{II} is the NH group directed away from the molecule (Ar@NH_{III}). The predicted ν_{OH} frequency is identical to that of the *cis*-H^+AI_I–Ar complexes. However, the splitting of the asymmetric ν_{NH} predicted to be 53 cm^{-1} is much smaller than the observed one. Moreover, the IRMPD spectrum at room temperature does not reveal any significant population of *cis*-H^+AI_{II}. Therefore, we assign the IRPD spectrum of *cis*-H^+AI–Ar mainly to a single isomer, namely the most stable Ar@NH_I isomer of *cis*-H^+AI_I–Ar, without definitively ruling out a slight contribution of higher energy isomers responsible for the shoulder observed at around 3340 cm^{-1}.

The calculated spectra of the *trans*-$H^+AI_{I/II}$ conformers with equatorial substituents fit the IR(M)PD spectra in Fig. 6 and 7 much better than those of the conformers with axial substituents (*trans*-$H^+AI_{III–V}$, Fig. S3 and S4 in the ESI†). In the NH stretch range, the asymmetric ν_{NH} frequencies are almost identical (3340 and 3336 cm^{-1}) for all three axial conformers (*trans*-$H^+AI_{III–V}$), whereas in the two equatorial *trans*-$H^+AI_{I/II}$ conformers, these ν_{NH} bands are well separated in frequency (Table 1, Fig. S3 in the ESI†). They are found at 3343 and 3320 cm^{-1} for *trans*-H^+AI_I, and at 3342 and 3314 cm^{-1} for *trans*-H^+AI_{II}, which fits well the experimental spectrum. These preliminary observations allow for ruling out significant contributions of axial conformers both at room temperature (IRMPD) and in the supersonic expansion (IRPD). Thus, as expected from the calculated energies, the eq–eq conformers are the only species identified in the gas phase.

In the fingerprint range, the spectra calculated for *trans*-H^+AI_I and *trans*-H^+AI_{II} do not permit the decision whether one or both equatorial conformers contribute to the experimental spectrum (Fig. 6). *trans*-H^+AI_I may provide a slightly better match with the experiment with respect to band positions and relative intensities, and its spectrum can reproduce all main features in the IRMPD spectrum. These observations may indicate that the IRMPD spectrum is dominated by the *trans*-H^+AI_I conformer, whereas contributions of *trans*-H^+AI_{II} are at most minor.

In the 3 μm range (Table 1, Fig. S3 in the ESI†), ν_{OH} is calculated to be 14 cm^{-1} lower in frequency for *trans*-H^+AI_{II} (3641 cm^{-1}) than for *trans*-H^+AI_I (3655 cm^{-1}). The experimental

ν_{OH} transition is observed as a single band at 3651 cm^{-1}, indicating that only one of the two conformers is present in the expansion, and its absolute value suggests the assignment to the more stable *trans*-H^+AI_I isomer. Additional calculations for *trans*-H^+AI_I–Ar clusters (Fig. S5 in ESI†) reveal that, similar to *cis*-H^+AI, Ar binds to the NH_3^+ group, which does not affect the ν_{OH} frequency. The calculated Ar binding energy to the OH group (6.6 kJ mol^{-1}) is much smaller than those to the NH groups (9.0–10.9 kJ mol^{-1}). Therefore, the experimental spectrum is attributed to *trans*-H^+AI_I–Ar with Ar bound to NH_3^+. In particular, the most stable and nearly isoenergetic *trans*-H^+AI_I–Ar@NH_I and H^+AI_I–Ar@NH_{II} isomers are thought to be responsible for the spectral splitting in the asymmetric ν_{NH} range, with peaks at 3328, 3316, and 3304 cm^{-1}. The match of the symmetric ν_{NH} measured to be 3240 cm^{-1} is also good with these two isomers. The broad and weak band at 3205 cm^{-1} may be due to a small contribution of the third *trans*-H^+AI_I–Ar@NH_{III} isomer, with Ar at the third NH group. In summary, the analysis of the IRPD spectrum of *trans*-H^+AI–Ar is fully consistent with the presence of the most stable *trans*-H^+AI_I conformer, which also fits the conclusion derived from the IRMPD spectrum.

The analysis of the vibrational spectra of *cis*- and *trans*-H^+AI recorded at room temperature in a trap on the one hand and in a cold supersonic expansion on the other hand results in identifying mainly a single conformer in both cases. This result is attributed to a large energy difference between the two most stable isomers predicted to be 4.6 kJ mol^{-1} for both diastereomers.

3.4. Vibrational spectroscopy of the AI^+ radical cations

The IRPD spectra recorded for the *cis*- and *trans*-AI^+–Ar radical cations in Fig. 8 are identical within experimental error. The spectrum of *trans*-AI^+ is recorded in a narrower range and displays a lower signal-to-noise ratio due to the higher melting point of *trans*-AI (~144 *vs.* ~120 °C). The rich spectra reveal a relatively large number of peaks, suggesting that several conformers are present. Despite being perhaps surprising at first sight, this observation is rationalised by the calculations, which predict that the alicyclic ring of neutral AI opens up upon ionisation leading to the formation of the same achiral non-rigid open structures for both diastereomers. The main bands appear at 3648, 3581, 3403, 3275, 3046, and 3010 cm^{-1}.

In Fig. 8, the experimental IRPD spectra of AI^+–Ar are compared to those calculated for the eight low-lying AI^+ conformers, which are located within 10 kJ mol^{-1} above the most stable isomer. The computed spectra shown in the figure are drawn to the same scale. It is immediately clear that none of the individual calculated spectra can account for all bands observed in the measured spectra. Indeed, all eight conformers are required to assign all measured transitions. The agreement is not perfect since it is likely that not all minima on the flat potential of the open cation are found. Finally, we note that the DFT calculations do not take into account the Ar tagging, which may induce additional minor spectral shifts and splittings and stabilise different AI^+ conformers to a different degree.[88–90] However, the analysis of the frequencies in terms of conformer families allows for disentangling the rich IRPD spectrum, providing a tentative but fully consistent assignment. In contrast to the neutral and protonated species it is perhaps not surprising to detect higher energy species for the radical cation. The AI^+ ions are formed by electron or chemical ionisation of *cis*-/*trans*-AI followed by ring opening, which releases a substantial amount of internal energy into the cation (>20 kJ mol^{-1}), which can then cool down by collisions into the many minima separated by low energy barriers.

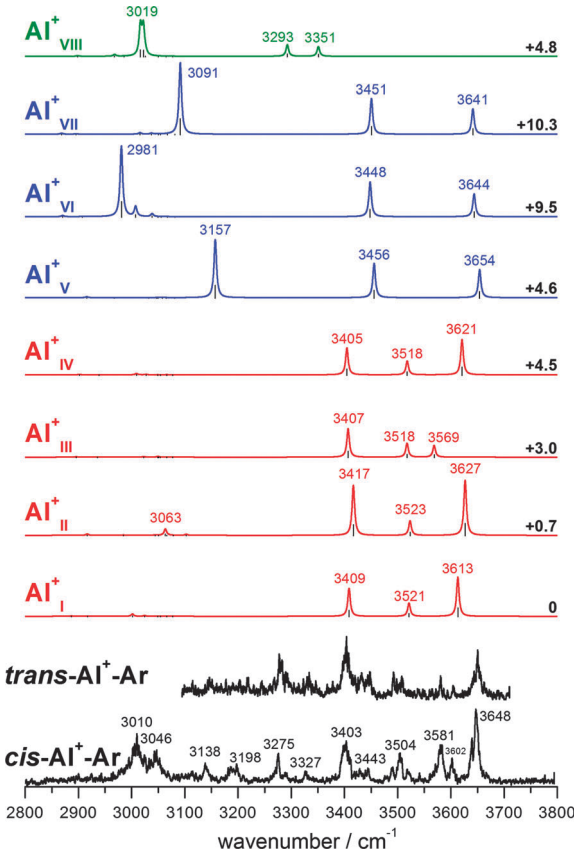

Fig. 8 IRPD spectra of *cis*-AI^+–Ar and *trans*-AI^+–Ar radical cation complexes compared to the vibrational IR spectra of the most stable open structures of AI^+ calculated at the B3LYP-D3/aug-cc-pVTZ level. Relative energies in kJ mol^{-1} are indicated on each spectrum.

Concerning the assignment of the IRPD spectra, the four most stable iminium isomers ($AI^+_{I–IV}$), which do not have intramolecular H-bonds, have quite similar IR spectra in the considered spectral range. Their ν_{OH} transitions are predicted between 3613 and 3627 cm^{-1}, except for AI^+_{III} for which it is calculated at 3569 cm^{-1}. Their asymmetric and symmetric ν_{NH} bands are located at around 3520 and 3410 cm^{-1}, respectively. This first group of non H-bonded conformers is therefore thought to be responsible for the peaks observed at 3602, 3581, 3504 and 3403 cm^{-1}. The second group of iminium structures, $AI^+_{V–VII}$, have an intramolecular NH···O H-bond and have calculated ν_{OH} transitions between 3641 and 3654 cm^{-1}, *i.e.* at higher frequency than the non H-bonded conformers. Moreover, their free ν_{NH} bands are located at around 3450 cm^{-1} and the H-bonded ν_{NH} are strongly red shifted to below 3160 cm^{-1}.

Thus, the peaks located at 3010, 3138, 3648 cm^{-1} and the broader feature at around 3430 cm^{-1} are attributed to this H-bonded conformer family. Finally, the last type of AI^+ structure (such as AI^+_{VIII}) has keto and ammonium functional groups. In this case, no ν_{OH} but the three ν_{NH} bands characteristic of the NH_3^+ group occur in the 3 μm range. For AI^+_{VIII}, a NH···O H-bond is predicted with a red shifted decoupled H-bonded ν_{NH} band at 3019 cm^{-1}. The two asymmetric free ν_{NH} are calculated at 3293 and 3351 cm^{-1}. This ammonium-type radical cation is then thought to give rise to the experimental bands at 3046, 3275, and 3327 cm^{-1}.

These qualitative assignments strongly support the conclusion that cleavage of the aliphatic ring occurs upon electron impact ionisation. The resulting floppy structure is responsible for the relatively rich IRPD spectra. It allows for identifying three main types of open structures, namely (i) the non H-bonded iminium type, (ii) the H-bonded iminium type with H-bonds between the iminium N–H group and the chain bearing the radical site, and (iii) a keto-ammonium type with a NH···O H-bond. All major peaks in the IRPD spectra can be rationalised by these conformer families.

4. Discussion

The two diastereomer molecules studied in this work differ by the relative position of the OH and NH_2 substituents, which is dictated by steric constraints in the alicyclic part of the molecules. In the *cis* form, the two functional groups are on the same side of the indane frame, which sterically favours the formation of the intramolecular H-bond. In the *trans* form, this interaction is not possible. Besides the presence or absence of the H-bond, the diastereomers also differ in the shape of the potential along the puckering motion, which has been shown to be very sensitive to small perturbations.[40,81,91,92] As a result, neutral *cis*- and *trans*-AI differ by the number of populated conformers under supersonic jet conditions. While the ax–eq and eq–ax positions of the OH–NH_2 substituents are isoenergetic in *cis*-AI, equatorial preference manifests itself by a large energy difference between the ax–ax and eq–eq conformations in *trans*-AI. The differences between *cis*- and *trans*-AI on the one hand and the two conformers I and II of *cis*-AI on the other hand are strongly reflected by their OH and NH stretch frequencies.

The NBO analysis can rationalise the shifts of the ν_{OH} and ν_{NH} modes, as reflected by the population of the antibonding σ*(OH) or σ*(NH) orbitals. To this end, we discuss the energetic contribution of the interactions between donor and acceptor NBOs, which has been estimated with second-order perturbation theory by means of the stabilisation energy E associated with delocalisation (Table 2).[93]

Surprisingly, the delocalisation of the H-bond acceptor lone pair (LP) towards the σ* orbital of the donor results in a smaller energy gain than its delocalisation to σ* orbitals localised on the aliphatic ring, either on CC or CH bonds, and called σ*(ali) hereafter. For example in *cis*-AI_I, the delocalisation of LP(N) into σ*(OH) is less important (E = 21.2 kJ mol^{-1}) than the delocalisation into σ*(ali) (E = 41.2 kJ mol^{-1}). This is also the case for *cis*-H^+AI_I: the delocalisation of $LP_1(O)$ into σ*(NH) results in a 7.0 kJ mol^{-1} stabilisation whereas the $LP_1(O)$ → σ*(ali) is stabilised by 14.8 kJ mol^{-1}. This result has already been reported for a cyclic amino-alcohol, (*S*)-1,2,3,4-tetrahydro-3-isoquinoline methanol (THIQM).[20] The second important aspect is that delocalisation takes place also from bonding σ(ali) orbitals localised on the alicyclic ring (σ(CC) or σ(CH)) into the σ*(NH) or σ*(OH) orbitals, influencing thereby the stretching frequency of the latter. In *cis*-AI_I, for example, the delocalisation of σ(ali) in σ*(NH) leads to a stabilisation of 18.4 kJ mol^{-1}.

Table 2 Stabilisation energies in kJ mol^{-1} associated with delocalisation between the donor and acceptor orbitals calculated at the B3LYP-D3/aug-cc-pVTZ level

Delocalisation[a]	*cis*-AI_I	*cis*-AI_{II}	*trans*-AI_I	*cis*-H^+AI_I	*cis*-H^+AI_{II}	*trans*-H^+AI_I
σ(ali) → σ*(NH)	18.4	14.8	22.8	19.7	19.3	22.8
σ(ali) → σ*(OH)	7.1	6.1	7.1	8.3	8.9	8.9
σ(NH) → σ*(ali)	19.0	18.1	23.9	15.7	18.7	19.3
σ(OH) → σ*(ali)	12.3	13.8	15.1	12.6	9.9	11.7
σ(NH) → σ*(OH)	0	0	0	0	2.2	0
LP(N) → σ*(ali)	41.2	39.5	48.6	—	—	—
LP(N) → σ*(OH)	21.2	22.4	0	—	—	—
$LP_1(O)$ → σ*(ali)	21.6	14.1	14.4	14.8	14.7	20.2
$LP_1(O)$ → σ*(NH)	0	0	0	7.0	18.1	0
$LP_2(O)$ → σ*(ali)	64.5	57.4	59.8	53.3	43.8	62.0
$LP_2(O)$ → σ*(NH)	0	0	0	0	4.6	0

[a] $\sigma^{(*)}$(ali) are the bonding and antibonding sigma orbitals of the bonds localised on the aliphatic rings ($\sigma^{(*)}$(CC) and $\sigma^{(*)}$(CH)), $\sigma^{(*)}$(NH) those of the amino/ammonium groups, $\sigma^{(*)}$(OH) those of the hydroxy group, LP(N) and $LP_{(1or2)}$(O) are the nitrogen and oxygen lone pairs, respectively.

The difference between *cis*- and *trans*-AI is mainly due to the presence or absence of the intramolecular H-bond, which involves a population transfer from LP(N) to the H-bonded σ*(OH) orbital (LP(N) → σ*(OH) in Table 2). The difference between the two *cis*-AI isomers I and II is more subtle and can be related to the cyclic nature of the molecule, which imposes constraints on the overlap between the electron donating and accepting orbitals and hence modifies their vibrational frequencies. The stabilisation energies reported in Table 2 allow for rationalising these effects. Neutral *cis*-AI_I and *cis*-AI_{II} differ in the way the σ*(NH) orbital is populated. In both cases, the contribution comes only from σ(ali), arising from C_NH and C_NC_O, where C_O (C_N) is the asymmetric carbon directly bonded to O (N). The delocalisation of σ(ali) leads to an energy of 3.6 kJ mol^{-1} higher in *cis*-AI_I than in *cis*-AI_{II}, which induces the substantially lower frequency of ν_{NH} experimentally observed and calculated in *cis*-AI_I. On the other hand, the main contribution to σ*(OH) stems from LP(N) but there is an additional contribution from σ(ali), arising from C_OH in *cis*-AI_I and from CC_O in *cis*-AI_{II}. A better overlap between σ*(OH) and σ(C_OH) than between σ*(OH) and σ(CC_O) enables more delocalisation in the former than in the latter, which explains the slightly smaller ν_{OH} frequency in *cis*-AI_I.

Protonation of *trans*-AI has little consequence, and the same non H-bonded conformer as in the neutral is observed. The effect of protonation is more prominent for *cis*-AI with a change

in the direction of the H-bond compared to the neutral. The NH···O interaction in the protonated form is stronger than the OH···N interaction in the neutral, because the NH_3^+ group is positively charged. The difference in the symmetric ν_{NH} frequencies between *trans*-H^+AI and *cis*-H^+AI is obviously related to the presence or absence of the H-bond. The H-bond results in an energy gain due to the delocalisation of LP(O) into σ*(NH) of 7.0 kJ mol^{-1}. More difficult to understand is the smaller ν_{OH} frequency in *trans*-H^+AI relative to *cis*-H^+AI. It can be explained in terms of a better delocalisation of $\sigma(C_OC_N)$ into the σ*(OH) orbital (E = 8.9 *vs.* 8.3 kJ mol^{-1}). This example confirms the high sensitivity of the vibrational frequencies on hyperconjugation.[20,94]

The difference in energy between *cis*-AI_I and *cis*-AI_{II} is more pronounced in the protonated species than in the neutral, with an energy gap of 4.6 kJ mol^{-1} in favour of *cis*-H^+AI_I. Therefore, for *cis*-H^+AI only one isomer is detected. The barrier between the two conformers *cis*-H^+AI_I and *cis*-H^+AI_{II} is calculated to be 4.0 kJ mol^{-1} (II → I, Fig. S6 in the ESI†), which enables their interconversion at room temperature and relaxation towards the most stable one, the energy difference being large enough for the population of conformer II to be negligible. The barrier is low enough for the interconversion to happen in the jet as well.[95]

As observed for the neutral, *cis*-H^+AI_I and *cis*-H^+AI_{II} show structural and spectroscopic differences. In particular, the less stable *cis*-H^+AI_{II} isomer surprisingly displays the stronger H-bond, with the shorter N···O and NH···O distances. Like in the neutral, the delocalisation involving the alicyclic ring orbitals σ*(ali) is of prime importance and explains this observation. Indeed, the C_O–C_N distance is longer in *cis*-H^+AI_{II} (1.558 Å) than in *cis*-H^+AI_I (1.544 Å) due to the population transfer from $\sigma(C_O–C_N)$ into σ*(OH) (8.9 kJ mol^{-1}) and σ*(NH) (5.9 kJ mol^{-1}), which are smaller in *cis*-H^+AI_I (8.3 and 5.5 kJ mol^{-1}, respectively). The shorter C_O–C_N distance in *cis*-H^+AI_I dictates in turn steric constraints on the H-bond, which prevent it from being optimal.

The same complex IRPD spectrum is observed for the *cis*- and *trans*-AI^+ radical cations. This is due to the fact that ionisation causes the ring to open up, which results in a floppy structure with a rich conformational landscape and the loss of the two chiral centres. Ionisation therefore induces the disappearance of chirality effects by ring opening. A similar loss of chirality upon ionisation has been observed before in amines, which become planar in the radical cation.[20]

5. Conclusion

(1*R*,2*S*)-*cis* and (1*R*,2*R*)-*trans* amino-indanol provide a peculiar case of an amino-alcohol, in which the formation of an intramolecular H-bond is strongly influenced by the relative chirality of the OH and NH_2 bearing carbons. While the formation of an OH···N H-bond would be possible in both (1*R*,2*S*) and (1*R*,2*R*) diastereomers of a linear 1-amino-2-alcohol, steric constraints due to the alicyclic ring make this interaction possible only in *cis*-AI and not in *trans*-AI. The vibrational frequency of the H-bond donor is strongly influenced by the formation of the H-bond, and to a smaller extent by hyperconjugation with σ* orbitals of the alicyclic ring. Ionisation leads to the opening of the alicyclic ring resulting in the loss of chirality for both chiral centres, C_O and C_N. As a result, the IR spectrum of the radical cation is identical, independent of whether it is formed from *cis*- or *trans*-AI. In contrast, the protonated species show the same chirality effect on H-bond formation as the neutral, which manifests itself by a different spectroscopic signature in the symmetric NH stretch range for *cis*- and *trans*-H^+AI. More subtle effects of chirality are also observed on the acceptor OH stretch frequency, due to chirality-dependent population transfer from the $\sigma(C_OC_N)$ orbital into the σ*(OH) orbital. Cyclic systems, by adding sterical constraints to those brought by chirality, therefore allow for sensitive detection of subtle stereochemical effects including the influence of chirality on hyperconjugation.

Acknowledgements

This work was supported by the Deutsche Forschungsgemeinschaft (DO 729/3), DAAD (ProCope, grant 55923144), MAEDI and MENESR (PHC Procope, Grant 28277SA). The research leading to these results has also received funding from the European Union's Seventh Framework Program (FP7/2012-2015) under grant agreement no. 312284 (CLIO project IC 14-019). A.B. has received funding from the People Programme (Marie Curie Actions) of the European Union's Seventh Framework Programme (FP7/2007-2013) under REA grant agreement no. 600209 (TU Berlin/IPODI). Thanks are due to Dr. Eric Gloaguen and Dr. Michel Broquier for helpful discussions.

References

1 R. Rometsch, *US pat.*, 2,957,880, 1960.
2 D. C. Warhurst, J. C. Craig, I. S. Adagu, D. J. Meyer and S. Y. Lee, *Malar. J.*, 2003, **2**, 26.
3 A. Zehnacker and M. A. Suhm, *Angew. Chem., Int. Ed.*, 2008, **47**, 6970.
4 *Chiral recognition in the Gas Phase*, ed. A. Zehnacker, CRC Press Taylor & Francis Group, Boca Raton, 2010.
5 D. Scuderi, K. Le Barbu-Debus and A. Zehnacker, *Phys. Chem. Chem. Phys.*, 2011, **13**, 17916.
6 A. Zehnacker, *Int. Rev. Phys. Chem.*, 2014, **33**, 151.
7 M. Speranza, M. Satta, S. Piccirillo, F. Rondino, A. Paladini, A. Giardini, A. Filippi and D. Catone, *Mass Spectrom. Rev.*, 2005, **24**, 588.
8 M. Speranza, F. Gasparrini, B. Botta, C. Villani, D. Subissati, C. Fraschetti and F. Subrizi, *Chirality*, 2009, **21**, 69.
9 M. Speranza, F. Rondino, M. Satta, A. Paladini, A. Giardini, D. Catone and S. Piccirillo, *Chirality*, 2009, **21**, 119.
10 W. A. Tao and R. G. Cooks, *Anal. Chem.*, 2003, **75**, 25A.
11 A. G. Abo-Riziq, J. E. Bushnell, B. Crews, M. P. Callahan, L. Grace and M. S. de Vries, *Int. J. Quantum Chem.*, 2005, **105**, 437.

12 E. Gloaguen, F. Pagliarulo, V. Brenner, W. Chin, F. Piuzzi, B. Tardivel and M. Mons, *Phys. Chem. Chem. Phys.*, 2007, **9**, 4491.
13 J. C. Dean, E. G. Buchanan, W. H. James, A. Gutberlet, B. Biswas, P. V. Ramachandran and T. S. Zwier, *J. Phys. Chem. A*, 2011, **115**, 8464.
14 P. Butz, R. T. Kroemer, N. A. Macleod, E. G. Robertson and J. P. Simons, *J. Phys. Chem. A*, 2001, **105**, 1050.
15 A. Sen, V. Lepere, K. Le Barbu-Debus and A. Zehnacker, *ChemPhysChem*, 2013, **14**, 3559.
16 A. Sen, A. Bouchet, V. Lepere, K. Le Barbu-Debus, D. Scuderi, F. Piuzzi and A. Zehnacker-Rentien, *J. Phys. Chem. A*, 2012, **116**, 8334.
17 R. C. Dunbar, J. D. Steill and J. Oomens, *J. Am. Chem. Soc.*, 2011, **133**, 1212.
18 M. E. Crestoni, B. Chiavarino, D. Scuderi, A. Di Marzio and S. Fornarini, *J. Phys. Chem. B*, 2012, **116**, 8771.
19 J. J. Lee, S. Hesse and M. A. Suhm, *J. Mol. Struct.*, 2010, **976**, 397.
20 A. Mahjoub, A. Chakraborty, V. Lepere, K. Le Barbu-Debus, N. Guchhait and A. Zehnacker, *Phys. Chem. Chem. Phys.*, 2009, **11**, 5160.
21 A. Chakraborty, N. Guchhait, K. Le Barbu-Debus, A. Mahjoub, V. Lepere and A. Zehnacker-Rentien, *J. Phys. Chem. A*, 2011, **115**, 9354.
22 A. Nontprasert, S. Pukrittayakamee, D. E. Kyle, S. Vanijanonta and N. J. White, *Trans. R. Soc. Trop. Med. Hyg.*, 1996, **90**, 553.
23 I. Gallou and C. H. Senanayake, *Chem. Rev.*, 2006, **106**, 2843.
24 K. Le Barbu-Debus, F. Lahmani, A. Zehnacker-Rentien and N. Guchhait, *Chem. Phys. Lett.*, 2006, **422**, 218.
25 K. Le Barbu-Debus, N. Guchhait and A. Zehnacker-Rentien, *Phys. Chem. Chem. Phys.*, 2007, **9**, 4465.
26 K. Le Barbu-Debus, M. Broquier, A. Mahjoub and A. Zehnacker-Rentien, *Phys. Chem. Chem. Phys.*, 2009, **11**, 7589.
27 A. D. Becke, *J. Chem. Phys.*, 1993, **98**, 5648.
28 M. J. Frisch, J. A. Pople and J. S. Binkley, *J. Chem. Phys.*, 1984, **80**, 3265.
29 S. Grimme, J. Antony, S. Ehrlich and H. Krieg, *J. Chem. Phys.*, 2010, **132**, 154104.
30 R. A. Kendall, T. H. Dunning and R. J. Harrison, *J. Chem. Phys.*, 1992, **96**, 6796.
31 M. J. Frisch, G. W. Trucks, H. B. Schlegel, G. E. Scuseria, M. A. Robb, J. R. Cheeseman, G. Scalmani, V. Barone, B. Mennucci, G. A. Petersson, H. Nakatsuji, M. Caricato, X. J. Li, H. P. Hratchian, A. F. Izmaylov, J. Bloino, G. Zheng, J. L. Sonnenberg, M. Hada, M. Ehara, K. Toyota, R. Fukuda, J. Hasegawa, M. Ishida, T. Nakajima, Y. Honda, O. Kitao, H. Nakai, T. Vreven, J. A. Montgomery, Jr., J. E. Peralta, F. Ogliaro, M. Bearpark, J. J. Heyd, E. Brothers, K. N. Kudin, V. N. Staroverov, R. Kobayashi, J. Normand, K. Raghavachari, A. Rendell, J. C. Burant, S. S. Iyengar, J. Tomasi, M. Cossi, N. Rega, J. M. Millam, M. Klene, J. E. Knox, J. B. Cross, V. Bakken, C. Adamo, J. Jaramillo, R. Gomperts, R. E. Stratmann, O. Yazyev, A. J. Austin, R. Cammi, C. Pomelli, J. W. Ochterski, R. L. Martin, K. Morokuma, V. G. Zakrzewski, G. A. Voth, P. Salvador, J. J. Dannenberg, S. Dapprich, A. D. Daniels, O. Farkas, J. B. Foresman, J. V. Ortiz, J. Cioslowski and D. J. S. Fox, *Gaussian 09*, Gaussian Inc, Wallingford, CT, 2009.
32 A. R. Allouche, *J. Comput. Chem.*, 2011, **32**, 174.
33 E. R. Johnson, S. Keinan, P. Mori-Sanchez, J. Contreras-Garcia, A. J. Cohen and W. Yang, *J. Am. Chem. Soc.*, 2010, **132**, 6498.
34 J. Contreras-Garcia, W. T. Yang and E. R. Johnson, *J. Phys. Chem. A*, 2011, **115**, 12983.
35 R. Chaudret, B. d. Courcy, J. Contreras-Garcia, E. Gloaguen, A. Zehnacker-Rentien, M. Mons and J. P. Piquemal, *Phys. Chem. Chem. Phys.*, 2014, **16**, 9876.
36 N. Seurre, K. Le Barbu-Debus, F. Lahmani, A. Zehnacker-Rentien and J. Sepiol, *Chem. Phys.*, 2003, **295**, 21.
37 N. Seurre, K. Le Barbu-Debus, F. Lahmani, A. Zehnacker-Rentien and J. Sepiol, *J. Mol. Struct.*, 2004, **692**, 127.
38 N. Seurre, K. Le Barbu-Debus, F. Lahmani, A. Zehnacker, N. Borho and M. A. Suhm, *Phys. Chem. Chem. Phys.*, 2006, **8**, 1007.
39 M. Albrecht, A. Borba, K. Le Barbu-Debus, B. Dittrich, R. Fausto, S. Grimme, A. Mahjoub, M. Nedic, U. Schmitt, L. Schrader, M. A. Suhm, A. Zehnacker-Rentien and J. Zischang, *New J. Chem.*, 2010, **34**, 1266.
40 J. Altnoeder, A. Bouchet, J. J. Lee, K. E. Otto, M. A. Suhm and A. Zehnacker-Rentien, *Phys. Chem. Chem. Phys.*, 2013, **15**, 10167.
41 C. Riehn, C. Lahmann, B. Wassermann and B. Brutschy, *Chem. Phys. Lett.*, 1992, **197**, 443.
42 S. Tanabe, T. Ebata, M. Fujii and N. Mikami, *Chem. Phys. Lett.*, 1993, **215**, 347.
43 R. N. Pribble and T. S. Zwier, *Science*, 1994, **265**, 75.
44 E. J. Bieske and O. Dopfer, *Chem. Rev.*, 2000, **100**, 3963.
45 M. Okumura, L. I. Yeh, J. D. Myers and Y. T. Lee, *J. Phys. Chem.*, 1990, **94**, 3416.
46 O. Dopfer, *Int. Rev. Phys. Chem.*, 2003, **22**, 437.
47 O. Dopfer, *Z. Phys. Chem.*, 2005, **219**, 125.
48 N. Solcà and O. Dopfer, *Chem. – Eur. J.*, 2003, **9**, 3154.
49 N. Solcà and O. Dopfer, *Angew. Chem., Int. Ed.*, 2002, **41**, 3628.
50 N. Solcà and O. Dopfer, *Angew. Chem., Int. Ed.*, 2003, **42**, 1537.
51 N. Solcà and O. Dopfer, *J. Phys. Chem. A*, 2005, **109**, 6174.
52 H. S. Andrei, S. A. Nizkorodov and O. Dopfer, *Angew. Chem.*, 2007, **119**, 4838.
53 H. S. Andrei, N. Solca and O. Dopfer, *Angew. Chem., Int. Ed.*, 2008, **47**, 395.
54 A. Patzer, S. Chakraborty, N. Solca and O. Dopfer, *Angew. Chem., Int. Ed.*, 2010, **49**, 10145.
55 A. Patzer, M. Schütz, T. Möller and O. Dopfer, *Angew. Chem., Int. Ed.*, 2012, **51**, 4925.
56 A. Patzer, M. Schütz, C. Jouvet and O. Dopfer, *J. Phys. Chem. A*, 2013, **117**, 9785.
57 A. Patzer, M. Zimmermann, I. Alata, C. Jouvet and O. Dopfer, *J. Phys. Chem. A*, 2010, **114**, 12600.
58 M. A. R. George, M. Savoca and O. Dopfer, *Chem. – Eur. J.*, 2013, **19**, 15315.

59 M. Savoca, M. A. R. George, J. Langer and O. Dopfer, *Phys. Chem. Chem. Phys.*, 2013, **15**, 2774.
60 M. Savoca, J. Langer and O. Dopfer, *Angew. Chem., Int. Ed.*, 2013, **52**, 1568.
61 J. Klyne, M. Schmies, M. Fujii and O. Dopfer, *J. Phys. Chem. B*, 2015, **119**, 1388.
62 J. Klyne, M. Schmies and O. Dopfer, *J. Phys. Chem. B*, 2014, **118**, 3005–3017.
63 K. Sakota, M. Schütz, M. Schmies, R. Moritz, A. Bouchet, T. Ikeda, Y. Kuono, H. Sekiya and O. Dopfer, *Phys. Chem. Chem. Phys.*, 2014, **16**, 3798.
64 K. Tanabe, M. Miyazaki, M. Schmies, A. Patzer, M. Schütz, H. Sekiya, M. Sakai, O. Dopfer and M. Fujii, *Angew. Chem., Int. Ed.*, 2012, **51**, 6604.
65 M. Schmies, M. Miyazaki, M. Fujii and O. Dopfer, *J. Chem. Phys.*, 2014, **141**, 214301.
66 M. Schmies, A. Patzer, M. Schütz, M. Miyazaki, M. Fujii and O. Dopfer, *Phys. Chem. Chem. Phys.*, 2014, **16**, 7980.
67 P. Maitre, S. Le Caer, A. Simon, W. Jones, J. Lemaire, H. Mestdagh, M. Heninger, G. Mauclaire, P. Boissel, R. Prazeres, F. Glotin and J. M. Ortega, *Nucl. Instrum. Methods Phys. Res., Sect. A*, 2003, **507**, 541.
68 G. Bouchoux, N. Choret, F. Berruyer-Penaud and R. Flammang, *Int. J. Mass Spectrom.*, 2002, **217**, 195.
69 B. Chiavarino, M. E. Crestoni, O. Dopfer, P. Maitre and S. Fornarini, *Angew. Chem., Int. Ed.*, 2012, **51**, 4947.
70 B. Chiavarino, M. E. Crestoni, M. Schuetz, A. Bouchet, S. Piccirillo, V. Steinmetz, O. Dopfer and S. Fornarini, *J. Phys. Chem. A*, 2014, **118**, 7130.
71 A. Lagutschenkov, R. K. Sinha, P. Maitre and O. Dopfer, *J. Phys. Chem. A*, 2010, **114**, 11053.
72 A. Lagutschenkov, U. J. Lorenz and O. Dopfer, *Int. J. Mass Spectrom.*, 2011, **308**, 316.
73 A. Lagutschenkov, A. Springer, U. J. Lorenz, P. Maitre and O. Dopfer, *J. Phys. Chem. A*, 2010, **114**, 2073.
74 A. Sen, K. Le Barbu-Debus, D. Scuderi and A. Zehnacker-Rentien, *Chirality*, 2013, **25**, 436.
75 D. Scuderi, V. Lepere, G. Piani, A. Bouchet and A. Zehnacker-Rentien, *J. Phys. Chem. Lett.*, 2014, **5**, 56.
76 G. Bouchoux and J. Y. Salpin, *Mass Spectrom. Rev.*, 2012, **31**, 353.
77 E. P. L. Hunter and S. G. Lias, *J. Phys. Chem. Ref. Data*, 1998, **27**, 413.
78 H. E. Audier, A. Milliet and J. P. Denhez, *Bull. Soc. Chim. Fr.*, 1983, 202.
79 A. Das, K. K. Mahato, S. S. Panja and T. Chakraborty, *J. Chem. Phys.*, 2003, **119**, 2523.
80 K. Le Barbu-Debus, F. Lahmani, A. Zehnacker-Rentien and N. Guchhait, *Phys. Chem. Chem. Phys.*, 2006, **8**, 1001.
81 Z. Arp, N. Meinander, J. Choo and J. Laane, *J. Chem. Phys.*, 2002, **116**, 6648.
82 E. B. Wilson, *J. Chem. Phys.*, 1939, **7**, 1047.
83 E. J. Bieske, S. A. Nizkorodov, O. Dopfer, J. P. Maier, R. J. Stickland, B. J. Cotterell and B. J. Howard, *Chem. Phys. Lett.*, 1996, **250**, 266.
84 O. Dopfer, S. A. Nizkorodov, M. Meuwly, E. J. Bieske and J. P. Maier, *Int. J. Mass Spectrom. Ion Processes*, 1997, **167–168**, 637.
85 N. M. Lakin, O. Dopfer, B. J. Howard and J. P. Maier, *Mol. Phys.*, 2000, **98**, 81.
86 N. M. Lakin, O. Dopfer, M. Meuwly, B. J. Howard and J. P. Maier, *Mol. Phys.*, 2000, **98**, 63.
87 N. M. Lakin, R. V. Olkhov and O. Dopfer, *Faraday Discuss.*, 2001, **118**, 455.
88 F. M. Pasker, N. Solca and O. Dopfer, *J. Phys. Chem. A*, 2006, **110**, 12793.
89 A. Bouchet, M. Schütz, B. Chiavarino, M. E. Crestoni, S. Fornarini and O. Dopfer, *Phys. Chem. Chem. Phys.*, 2015, **17**, DOI: 10.1039/C5CP00221D.
90 N. Solca and O. Dopfer, *J. Chem. Phys.*, 2004, **120**, 10470.
91 A. Bouchet, J. Altnoder, M. Broquier and A. Zehnacker, *J. Mol. Struct.*, 2014, **1076**, 344.
92 Y. Loquais, PhD thesis, Univ. Paris Sud, 2013.
93 A. E. Reed, L. A. Curtiss and F. Weinhold, *Chem. Rev.*, 1988, **88**, 899.
94 E. Gloaguen, V. Brenner, M. Alauddin, B. Tardivel, M. Mons, A. Zehnacker-Rentien, V. Declerck and D. J. Aitken, *Angew. Chem., Int. Ed.*, 2014, **53**, 1.
95 R. S. Ruoff, T. D. Klots, T. Emilsson and H. S. Gutowsky, *J. Chem. Phys.*, 1990, **93**, 3142.